Use of High-Resolution Satellite Observations to Evaluate Cloud and Precipitation Statistics from Cloud-Resolving Model Simulations. Part I: South China Sea Monsoon Experiment

Y. P. ZHOU,* W.-K. TAO,+ A. Y. HOU,+ W. S. OLSON,# C.-L. SHIE,* K.-M. LAU,+ M.-D. CHOU,@ X. LIN,* AND M. GRECU*

*Goddard Earth Sciences and Technology Center, University of Maryland, Baltimore County, Baltimore, Maryland
+NASA Goddard Space Flight Center, Greenbelt, Maryland
#Joint Center for Earth Systems Technology, University of Maryland, Baltimore County, Baltimore, Maryland
@National Taiwan University, Taipei, Taiwan

(Manuscript received 25 August 2006, in final form 20 February 2007)

ABSTRACT

Cloud and precipitation simulated using the three-dimensional (3D) Goddard Cumulus Ensemble (GCE) model are compared to Tropical Rainfall Measuring Mission (TRMM) Microwave Imager (TMI) and Precipitation Radar (PR) rainfall measurements and Clouds and the Earth's Radiant Energy System (CERES) single scanner footprint (SSF) radiation and cloud retrievals. Both the model simulation and retrieved parameters are based upon observations made during the South China Sea Monsoon Experiment (SCSMEX) field campaign. The model-simulated cloud and rain systems are evaluated by systematically examining important parameters such as the surface rain rate, convective/stratiform percentage, rain profiles, cloud properties, and precipitation efficiency.

It is demonstrated that the GCE model is capable of simulating major convective system development and reproduces the total surface rainfall amount as compared to rainfall estimated from the SCSMEX sounding network. The model yields a slightly higher total convective rain/stratiform rain ratio than the TMI and PR observations. The GCE rainfall spectrum exhibits a greater contribution from heavy rains than those estimated from PR or TMI observations. In addition, the GCE simulation produces much greater amounts of snow and graupel than the TRMM retrievals. The model's precipitation efficiency of convective rain is close to the observations, but the precipitation efficiency of stratiform rain is much lower than the observations because of large amounts of slowly falling simulated snow and graupel. Compared to observations, the GCE produces more compact areas of intense convection and less anvil cloud, which are consistent with a smaller total cloud fraction and larger domain-averaged outgoing longwave radiation.

1. Introduction

Clouds and precipitation play key roles in linking the earth's energy cycle and water cycles. Clouds modulate the incoming solar radiation through reflection and the outgoing longwave radiation by altering the effective emitting temperature. Cloud itself is an important component of the hydrological cycle. Precipitation starts with cloud formation and through condensation and latent heat release it connects both the energy and water cycles. The sensitivity of deep convective cloud systems and their associated precipitation efficiency in response to climate change are key factors in predicting the future climate.

Components of the space-based Earth Observing System (EOS), such as the National Aeronautics and Space Administration's (NASA) Clouds and the Earth's Radiant Energy System (CERES) experiment (Wielicki et al. 1996) and the Tropical Rainfall Measuring Mission (TRMM; Simpson et al. 1988, 1996) are designed to provide crucial cloud and precipitation measurements for advancing our understanding of the role of clouds and precipitation in the global energy and water cycles, and for improving their representation in general circulation and climate models. The CERES products include broadband shortwave and longwave radiation from the top of the atmosphere, as well as simultaneous cloud properties retrieved from the other

Corresponding author address: Dr. Yaping Zhou, NASA Goddard Space Flight Center, Mail Code 613.2, Greenbelt, MD 20771. E-mail: yaping.zhou-1@nasa.gov

DOI: 10.1175/2007JAS2281.1

instruments. The TRMM instruments provide comprehensive measurements of precipitation variation and properties such as surface rain rate, the vertical structure of precipitation, and latent heating. Simultaneous cloud and precipitation measurements provide unprecedented capabilities for studying the large-scale, aggregate effects of cloud and precipitation systems.

Cloud and precipitation processes are controlled by large-scale dynamics, convection, and microphysical processes. The use of satellite data to study the relationship between cloud and precipitation and the effects of the different controlling mechanisms is a very complicated problem because of the wide range of scales and types of cloud systems involved. Cloud-resolving (or cumulus ensemble) models (CRMs) can simulate the conversion of cloud condensate into raindrops and various forms of precipitation in great detail. CRMs have been used to simulate individual clouds as well as organized mesoscale convective systems (MCS; Tao and Simpson 1989; Skamarock et al. 1994; Parker and Johnson 2004; and many others). In recent years, CRMs have become one of the primary tools to develop the physical parameterizations of moist and other subgrid-scale processes in global circulation and climate models (Randall et al. 1996). Randall et al. (2003) further suggested that CRMs should be used as a replacement of traditional cloud parameterizations in GCMs. In their pioneering work, Khairoutdinov et al. (2005) have embedded a CRM into each grid column of the National Center for Atmospheric Research (NCAR) Community Atmosphere Model (CAM) to serve as a superparameterization (SP) of clouds, and found improvements in the model's simulation of precipitation frequency. Meanwhile, a prototype Goddard Multiscale Modeling Framework (MMF) is being developed using the 2D Goddard Cumulus Ensemble (GCE) model embedded in the Goddard finite volume General Circulation Model (fvGCM), replacing the cumulus parameterization in the fvGCM (Tao et al. 2008). However, CRMs still need parameterizations on scales smaller than their grid resolutions and have many known and unknown deficiencies. If CRMs are to fulfill these important applications, they must be tested against observations for various dynamical environments and cloud–rain system types. The robustness of CRMs in simulating cloud and rain processes given known environmental conditions is one of the most important requirements for them to be useful.

The use of CRMs in the study of tropical convection and its relation to the large-scale environment is called "cloud ensemble modeling" approach. In this approach, many clouds/cloud systems of different sizes in various stages of their life cycles can be present at any model simulation time. The model is driven by large-scale advective forcing in temperature and water vapor usually derived from intensive sounding networks deployed during major field experiments (Soong and Ogura 1980; Tao and Soong 1986; and many others). In addition, the cloud ensemble models use cyclic lateral boundary conditions (to avoid reflection of gravity waves) and require a large horizontal domain (to allow for the existence of an ensemble of clouds). The advantage of this approach is that the modeled convection will produce the same (but not identical) intensity, thermodynamic budget, and organization as the observations. This approach also allows the CRM to perform multiday or multiweek time integrations. The CRM, then, can be use to obtain enough samples to compute the statistical properties of clouds/cloud systems. This type of cloud-resolving modeling has been used in many modeling studies for studying the South China Sea Monsoon Experiment (SCSMEX), the Global Atmospheric Research Program (GARP) Atlantic Tropical Experiment (GATE), the Tropical Ocean Global Atmosphere Coupled Ocean–Atmosphere Response Experiment (TOGA COARE), and the Department of Energy/Atmospheric Radiation Measurement Program/Southern Great Plains site (DOE/ARM/SGP) convective systems (Soong and Tao 1984; Lipps and Hemler 1986; Krueger 1988; Xu and Randall 1996; Wu et al. 1998, 1999; Grabowski et al. 1996, 1998; Li et al. 2002; Donner et al. 1999; Petch and Gray 2001; Xu et al. 2002; Johnson et al. 2002; Tao et al. 2003a; and many others). Please see Moncrieff et al. (1997) and Tao et al. (2003b) for brief review.

Validation of CRMs is usually performed using bulk energy and water budgets in these long-term model integrations, however. Direct comparison of CRM simulations with low earth-orbiting satellite data is difficult because such satellite data only provide limited snapshots of a limited area (scale <1000 km) at a given time. Recently, Eitzen and Xu (2005) compared cloud properties of deep convective cloud objects from satellite and CRM simulations using probability distribution functions (PDFs) by simulating a large number of cloud objects using corresponding large-scale forcing data from European Centre for Medium-Range Weather Forecasts (ECMWF) reanalyses. The deep convective cloud object in their study is defined as a contiguous region of footprints with cloud optical thickness greater than 10, cloud height greater than 10 km, and 100% cloudy conditions within each footprint. Their simulations are only run for 24 h for each cloud object using a 2D model. While this method provides a large number of cloud objects for different times and loca-

TABLE 1. The TRMM instruments and observed parameters used in the study.

Instrument	Parameters	Resolution	Swath	No. of overpasses	Total pixels
TMI	Surface rain rate, convective rain rate, hydrometeor profiles	14 km	760 km	53	1.1×10^6
PR	Surface rain rate, rain type, radar reflectivity, Etop	4.3 km	215 km	53	5.3×10^5
CERES	Broadband SW, LW	10 km	700 km	57	4.9×10^5
VIRS	Cloud fraction, optical thickness, cloud top, etc.	2.2 km	720 km	57	4.9×10^5

tions, it is hard to evaluate how the model simulates entire synoptic systems.

In this study, we will examine the cloud and precipitation properties observed from the CERES and TRMM instruments against simulation from the 3D GCE model over the SCSMEX Northern Enhanced Sounding Array (NESA; Lau et al. 2000). Comparisons over other field experiment sites are undergoing and will be reported later. The comparison of cloud and precipitation from GCE simulation and satellite retrievals will serve two purposes. First, GCE has been used to perform long-term integrations to provide cloud datasets associated with various types of clouds/cloud systems from different geographic locations for TRMM precipitation retrieval algorithms (Simpson et al. 1996). It has also been used in the TRMM algorithms to provide a link between latent heating profiles and TRMM Microwave Imager (TMI) and precipitation radar (PR) observations, because latent heating cannot be directly measured. Comparing GCE simulations with TMI retrievals provides a consistent check of the model and retrievals under different environmental conditions. Second, combined cloud and precipitation measurements from independent instruments provide a more complete picture of the cloud system, which aids the implementation of more realistic and complete physics for model improvement. The SCSMEX experiment, conducted in May–June 1998, was one of the four major TRMM field campaigns aimed at the validation of TRMM products (i.e., rainfall and the vertical distribution of latent heating). These field campaigns provided observations of the structure and evolution of MCSs, individual convective clouds, and their large-scale environments for deriving large-scale forcing/initial conditions for CRM simulations and their validation. The SCSMEX experiment, in particular, was designed to understand the key physical processes associated with the onset and evolution of the summer monsoon over South Asia and southern China (Lau et al. 2000).

In this paper, the 3D GCE model is set up to perform a 30-day SCSMEX simulation. A 2D GCE simulation of two subset periods from 18–26 May and 2–11 June was reported in Tao et al. (2003a) with an emphasis on temporal variation and domain-averaged heating and moisture budgets. In this study, the model-simulated cloud and precipitation are compared statistically with CERES and TRMM observations. The similarities and discrepancies in the statistics of precipitation and cloud fields will be discussed in detail. In section 2, the TRMM data used in this study are described and a brief discussion of the comparability between the CRM simulation and satellite data is given. The model and model setup are discussed in section 3. The results from comparisons are shown and discussed in section 4. A summary of this work is given in section 5.

2. Satellite data

The TRMM satellite was launched in 1997 carrying the PR, the first spaceborne weather radar, together with the TMI, the Visible and Infrared Scanner (VIRS), the Lightning Imaging Sensor (LIS), and a CERES instrument. Products from four of the instruments onboard the TRMM satellite are used in this study (Table 1). They are CERES broadband shortwave (SW) and longwave (LW) radiation, cloud properties derived from VIRS, and surface rain-rate and hydrometeor profiles from TMI and PR.

In the CERES single scanner footprint (SSF) product, the 10-km-resolution CERES broadband measurements are collocated with higher resolution narrowband cloud retrievals from VIRS. Both instruments cover about a 700-km swath. The broadband SW and LW radiative fluxes in the CERES SSF dataset are estimated using the new angular distribution models (ADMs) for specific cloudy/clear atmosphere types (Loeb et al. 2003). Cloud properties (e.g., cloud fraction, optical thickness, cloud effective height, temperature) are retrieved from the VIRS cloud imager and averaged over the larger (10 km) CERES footprints (Minnis et al. 1997).

The TRMM TMI version 6 2A12 products (Kummerow et al. 2001; Olson et al. 2006) provide surface rainfall and 3D structure of hydrometeors and heating over the TMI swath in 14 vertical layers. The algorithm for generating the 2A12 products [often referred to as the Goddard Profiling (GPROF; Kummerow et al.

2001)] uses a Bayesian methodology to relate the observed multichannel brightness temperatures to a prior database of hydrometeors simulated by cloud-resolving models with explicit cloud microphysics. The TMI retrieval is limited by the simulated cloud sample distributions as well as microphysics in the cloud-resolving models. One of the cloud-resolving models used for generating the original database is the GCE model [the others are the fifth-generation Pennsylvania State University (PSU)–NCAR Mesoscale Model (MM5) and the University of Wisconsin Nonhydrostatic Modeling System (Tripoli 1992)], and all simulations use the GCE bulk microphysics scheme; therefore the TMI retrievals are expected to have some similarity to the GCE simulation. Besides surface rainfall and hydrometeor profiles (vertical distributions of cloud liquid, cloud ice, rain, and precipitating ice) for each radiometer footprint, the TMI algorithm estimates the fraction of convective rain relative to the total surface rain.

The TRMM PR is an electronically scanning radar, operating at 13.8 GHz, that measures the 3D rainfall distributions over both land and ocean surfaces (Kummerow et al. 1998). The PR scans 17° to either side of nadir at intervals of 0.35°, giving a vertical resolution of 250 m, a swath width of 215 km, and a horizontal footprint of 4.3 km at nadir. The PR swath is much narrower than the TMI swath (760 km), but is centered in the TMI swath. The PR estimates of attenuation-corrected radar reflectivity factor and rainfall rate are given at each resolution cell (4 km $\times$ 4 km $\times$ 250 m) of the radar. The estimated near-surface rainfall rate and average rainfall rate between the two predefined altitudes (2 and 4 km) are also calculated for each radar beam position. In this study, the PR instantaneous three-dimensional distribution of rain rate (2A-25 product) and rain classification (2A-23 product) are utilized.

Direct comparisons of CRM simulations and satellite data are difficult because the satellite only provides limited "snapshots" of a $\leq$1000-km-scale region at a given time. The TRMM satellite operates at an altitude of 350 km and 35° inclination orbit, requiring 46 days to complete one precession cycle. In this study, about 53 TRMM overpasses covering or partially covering the SCSMEX domain (17°–24°N, 108°–124°E) during the GCE simulation period (18 May–18 June 1998) are collected. Overpasses that cover less than one-third of its maximum coverage in the SCSMEX domain are discarded for their possible large bias relative to the domain-averaged quantities. The total pixels from the GCE simulation period for each instrument are listed in Table 1. This amounts to over a million total TMI pixels and half a million PR pixels collected over the domain during this time period. There are also nearly half a million CERES footprints collected for assessing the cloud statistics. Since cloud and precipitation systems evolve on time scales of hours, polar orbiting satellites cannot provide accurate process diagnostic means for individual cloud precipitation processes. On the other hand, given large enough samples, satellite observations are able to represent different cloud and precipitation systems in various stages of development, and observe some of the basic physical relations and structural patterns for similar cloud and precipitation types. Furthermore, since GCE is driven by observed large-scale advective forcings of potential temperature, water vapor mixing ratio, and horizontal momentum in a semiprognostic manner, the response of cloud microphysics (precipitation, condensation) is directly proportional to the large-scale forcing (Soong and Tao 1980). Therefore the model is expected to reproduce the rain and cloud statistics reasonably close to the observations. However, it is not clear if the model can produce the vertical structure of cloud and precipitation particles realistically because of the scarcity of high-quality observations.

3. The Goddard Cumulus Ensemble model and model setups

a. The GCE model

The model used in this study is the 3D version of the GCE model. The equations that govern cloud-scale motion (wind) are anelastic (sound waves are filtered). The subgrid-scale turbulence scheme used in the GCE model is based on work by Klemp and Wilhelmson (1978) and modified by Soong and Ogura (1980) by including the effects of condensation on the generation of subgrid-scale kinetic energy. The cloud microphysics includes a parameterized two-category liquid hydrometeor scheme (cloud water and rain), and a parameterized Lin et al. (1983) and Rutledge and Hobbs (1984) three-category ice-phase hydrometeor scheme (cloud ice, snow, and graupel). Shortwave (solar) and longwave (infrared) radiation parameterizations are also included in the model (Tao et al. 1996). The TOGA COARE bulk flux algorithm (Fairall et al. 1996) is linked to the GCE model for calculating surface fluxes over ocean (Wang et al. 1996). All scalar variables (potential temperature, mixing ratio of water vapor, turbulence coefficients, and all five hydrometeor classes) use forward time differencing and a positive definite advection scheme with a nonoscillatory option (Smolarkiewicz and Grabowski 1990). The dynamic variables u, v, and w use a fourth-order accurate advection scheme and a leapfrog time integration (kinetic energy

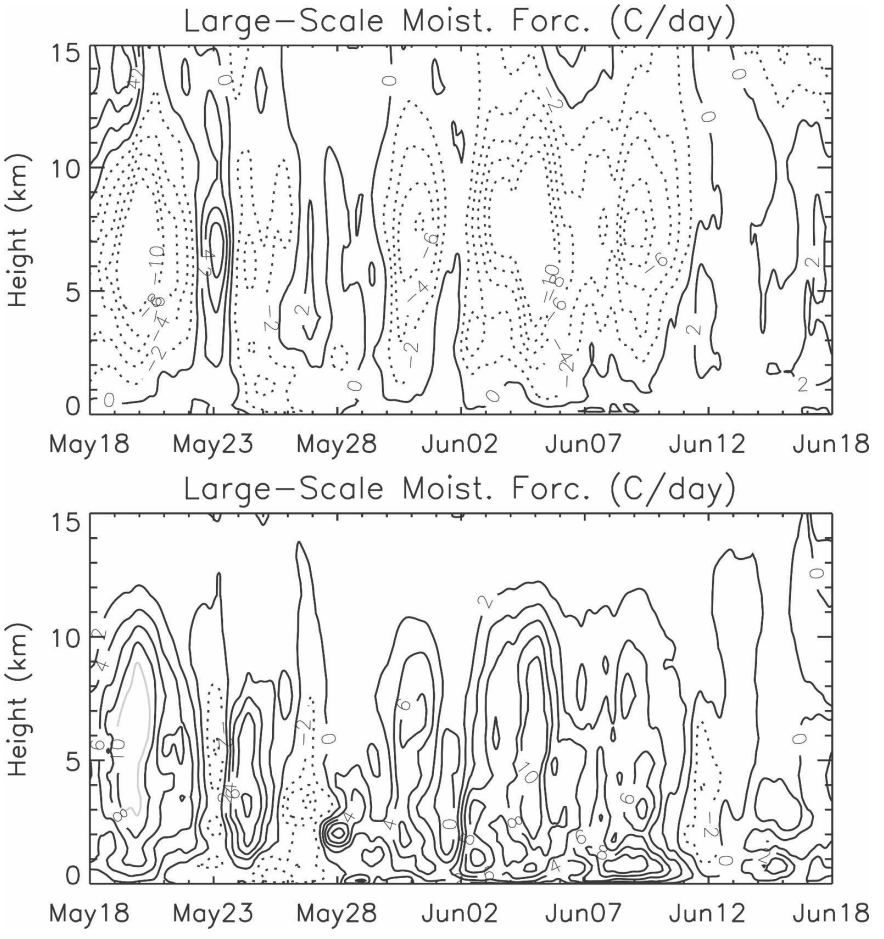

FIG. 1. Large-scale forcing of (top) temperature and (bottom) moisture for 18 May–18 Jun 1998.

semiconserving method). Details of the GCE model description and improvements can be found in Tao and Simpson (1993) and Tao et al. (2003b).

b. Model setup

In the simulation of this study, the 3D model has a stretched vertical coordinate of 32 levels with height increments from 143 m in the boundary layer to 1164 m near the model top. The model horizontal grid is 256 × 256 with a uniform grid spacing of 2-km resolution, yielding a 512 km × 512 km domain. The time step is 12 s, and the rain and atmospheric profiles are sampled at every hour of simulation time. When comparing with satellite data, the model output is averaged into 4-, 14-, and 10-km spatial resolutions to be consistent with spatial resolutions of PR, TMI, and CERES SSF, respectively. A few boundary grids are left out for 14- and 10-km averages.

The observed large-scale advective forcing of temperature and moisture over the SCSMEX domain for the simulation period was analyzed by Johnson and Ciesielski (2002) as shown in Fig. 1. Two major convective events around 18–26 May and 2–11 June 1998 can be identified during this period with strong cooling and moisture convergence. The first event is prior to and during the onset of the monsoon; the second is post onset. Both events show a similar order of magnitude of peak heating between 5 and 10 km. The June event has stronger forcing in both temperature and water vapor (see Tao et al. 2003a).

c. Cloud area, convective–stratiform partitioning methods

In the GCE model, as well as in satellite observations, a prescribed threshold is needed in order to define a "cloudy" location, since the transition from pristine atmosphere to cloudy atmosphere is gradual. Satellite observations usually use visible and IR threshold

methods to define a cloudy footprint. The CERES cloud fraction is defined for each 10-km-resolution CERES footprint using the 2-km-resolution VIRS instrument as the ratio of cloudy VIRS versus total VIRS pixels within the footprint.

In GCE, a cloudy grid location is defined as one if the total cloud hydrometeor mixing ratio exceeds a certain threshold. The threshold is somewhat arbitrary unless it is constrained by the observations. Sui et al. (1994) chose 0.005 g kg^{-1} as a threshold for any vertical layer; that is, the grid location was considered cloudy if any of the grid elements in the vertical column satisfied the threshold. In this study, we will test total hydrometeor threshold of 0.002, 0.005, and 0.008 g kg^{-1} to examine the sensitivity of the cloudy classification on this threshold. Moreover, we will use a threshold optical thickness of 0.3 to classify a cloudy grid since detectable cloud from CERES instruments has minimum optical thickness of 0.3, so that the model cloud fraction is optically equivalent to the CERES cloud fraction. In addition, an effective cloud top is defined as the level where the optical thickness reaches one when looking downward from the top of the model atmosphere; this definition is comparable to the definition of satellite effective cloud height.

The convective and stratiform rain partitioning techniques used for the GCE model output and satellite observations have some similarities but are based on different algorithms. The PR algorithm uses two different methods for classifying rain type; one is a vertical profile method (V method), and the other is a horizontal pattern method (H method; Awaka et al. 1998). The V method is based on detection of brightness band (BB) and a convective threshold. The H method is based upon an analysis of the horizontal pattern of maximum radar reflectivity (Zmax) developed by Steiner et al. (1995). Both methods classify rain into three categories: stratiform, convective, and other. The final results are combinations of the two methods.

Because of TMI's lower resolution, a convective area fraction is computed for each TMI footprint. The algorithm uses the local horizontal gradients (or texture) of the brightness temperatures (Hong et al. 1999) as well as the polarization of 85.5-GHz scattering signatures (Olson et al. 2001). The texture and polarization-based estimates of convective area fraction within a TMI footprint are merged by taking a weighted average of the estimates.

In GCE, each grid box is also classified as clear, stratiform, convective, or stratiform without surface rain. First, the convective, stratiform, and no-surface-precipitation regions are identified using the information from surface rain rates (Churchill and Houze 1984). Two additional criteria are then applied, which have been included to identify regions where convection may be quite active aloft though there is little or no precipitation yet at the surface, such as areas associated with tilted updrafts and new cells initiated ahead of an organized squall line (Tao and Simpson 1989; Tao et al. 1993). Different convective and stratiform separation techniques (Churchill and Houze 1984; Tao et al. 1993; Xu 1995; Caniaux et al. 1994; Steiner et al. 1995) were examined and compared by Lang et al. (2003).

4. Results

a. General features

It is not expected that the GCE simulation will match the satellite observations spacewise and timewise. The GCE model is intended to simulate the collective effects of cloud systems. It is also driven by horizontally uniform large-scale forcing that is computed over a domain that is larger than the simulation domain. On the other hand, the response of cloud microphysics (precipitation and condensation) is directly proportional to the large-scale forcing. Therefore, the model is expected to reproduce rain and cloud fields that are statistically similar to the observations.

Figures 2a and 2b show snapshots of surface rainfall from TMI measurements, outgoing longwave radiation (OLR), cloud optical thickness, and cloud-top pressure from the CERES and VIRS instruments, as well as the corresponding GCE simulation at the same time. Note that the domain size of GCE simulation is approximately $5° \times 5°$ but the satellite images show a domain size of $16° \times 10°$ from which the large-scale forcing is derived. The reason we chose a $5° \times 5°$ model domain size is because a larger domain size with the same spatial resolution is computationally more expensive, and the simulation using the $5° \times 5°$ domain is quite representative of the cloud systems in a larger domain, as our sensitivity studies indicate (figures not shown). While the satellite images show an organized mesoscale convective rain system at approximately 0800 UTC 19 May, the precipitation from the GCE simulation is quite intense but less organized in that there are many isolated cells of heavy rain and only slight evidence of linear organization in the upper-right portion of the domain (Fig. 2a). Note that the precipitation cells in the GCE simulation have horizontal scales ~10–20 km and do not represent individual cloud updrafts. The OLR, cloud optical thickness, and top pressure from CERES show deep convective cores with low OLR and high optical thickness surrounded by gradually thinning anvil clouds. The OLR from the GCE simulation shows large areas of high infrared emission aside from the

locations of precipitation cells. GCE optical thicknesses higher than CERES optical thicknesses are found, but these are limited to the raining areas, indicating that cloud in the GCE simulation is highly concentrated in raining areas, and the model probably does not produce enough anvil cloud. Figure 2b shows a better organized MCS at 1600 UTC4 June from both satellite observations and the GCE simulation. The model again produces small cells of intense precipitation with higher cloud tops (lower top pressure), larger optical thicknesses, and lower OLR, but these precipitation cells are grouped in a large mesoscale "cluster." It is well known that the organization of tropical convection is influenced predominantly by the vertical shear and convective available potential energy (CAPE; Moncrieff and Green 1972; Alexander and Young 1992; Keenan and Carbone 1992; LeMone et al. 1998; Tao et al. 1999; Shie et al. 2003). Johnson et al. (2005) recently examined in detail the organizational modes of convection over the northern South China Sea in relation to low- and midlevel wind shears. The organization of convection in GCE is apparently affected by environmental wind shear, as these two cases demonstrate: the zonal wind on 19 May had a unidirectional shear profile while on 4 June the zonal shear reversed sign with altitude (Fig. 3). The former shear profile is related to unicell-type convection (Dudhia et al. 1987; Tao et al. 2003a) and a weak mesoscale circulation, while the latter type of shear generally corresponds to multicell-type convection and a stronger mesoscale circulation. Overall, the model simulates the time variation of surface rainfall quite well upon inspection of each overpass image and corresponding GCE simulation. In the following section, more detailed comparisons will be conducted for surface rainfall, vertical structure of cloud and rain, and rain efficiency.

b. Surface rainfall characteristics

Presented in Fig. 4 are the time series of surface rainfall rates averaged over the SCSMEX region that are simulated by the GCE model and estimated from TMI and PR, as well as from soundings. The temporal variation of the GCE-model-simulated rainfall is in good agreement with that estimated from the water vapor budget determined from the soundings except that the GCE produces slightly less rainfall than the sounding estimates most of the time. The GCE simulation captures the two major convective periods, 18–26 May (during the monsoon onset) and 2–11 June (after the monsoon onset). The large-scale forcing in water vapor is much stronger in the June episode than in the May episode (Fig. 1); therefore the model's precipitation production in June is stronger than in May. The domain-averaged rainfall from PR is quite close to both the sounding and GCE rainfall, but TMI seems to underestimate the heavy rainfall events during the June episode simulated by the model. The TMI also underestimates relative to the sounding and PR measurements, but not during the May episode. One of the reasons might be that TMI tends to underestimate high rainfall rates because of the lack of sensitivity of microwave radiances to changes in rain rate at these high rates, coupled with the fact that the convection is generally stronger in the June episode than in the May episode. The mean simulated rainfall for the period is 10.2 mm day^{-1}, which is 11% lower than the sounding estimates and 23% higher than the TMI rainfall (Table 2). The 3D GCE simulations of rainfall are very close to those simulated by the 2D model in Tao et al. (2003a) with slightly lower total rainfall and higher convective rain ratio. It must be noted that the domain of the GCE simulation is about $5° \times 5°$, while the satellite observations are averaged over a larger domain ($16° \times 10°$) where the forcing is derived. TMI and PR overpasses only partially cover that domain (e.g., Fig. 2); the sampling of the domain by the PR is especially limited, since its swath is only a third of the width of the TMI's. Therefore, which precipitation estimates are more representative of the truth is a debatable point, since all methods involve different sampling and retrieval limitations. PR is considered to yield the best rainfall estimates, but it is limited by its narrow swath. Even the rainfall from soundings is limited by their 6-hourly temporal sampling, considering the relatively rapid evolution of convective systems. Another problem with the satellite data is their uneven temporal and spatial sampling. Because of the precession of the TRMM satellite orbit, the local overpass time over the domain is not fixed, as is the percentage of the domain area that is sampled. This could bias the results if the number of orbits processed is not large enough.

It is the purpose of this study to compare the GCE rainfall and satellite rainfall in more detail, beyond the total and domain averages, so that we can link the detailed rain and cloud structures with cloud microphysics in the model. Listed in Table 3 are additional rain statistics from the GCE simulation as well as those from the TMI and PR measurements. The GCE "overpass samples" are taken from corresponding TMI overpass times; "all data" are sampled every hour. The GCE rainfall data are spatially averaged to 4- and 14-km resolution, corresponding to the PR and TMI spatial resolutions, respectively. The statistics from the GCE overpass samples and all data are very similar, indicating that these overpass samples are sufficient to represent the precipitation over the whole period from the

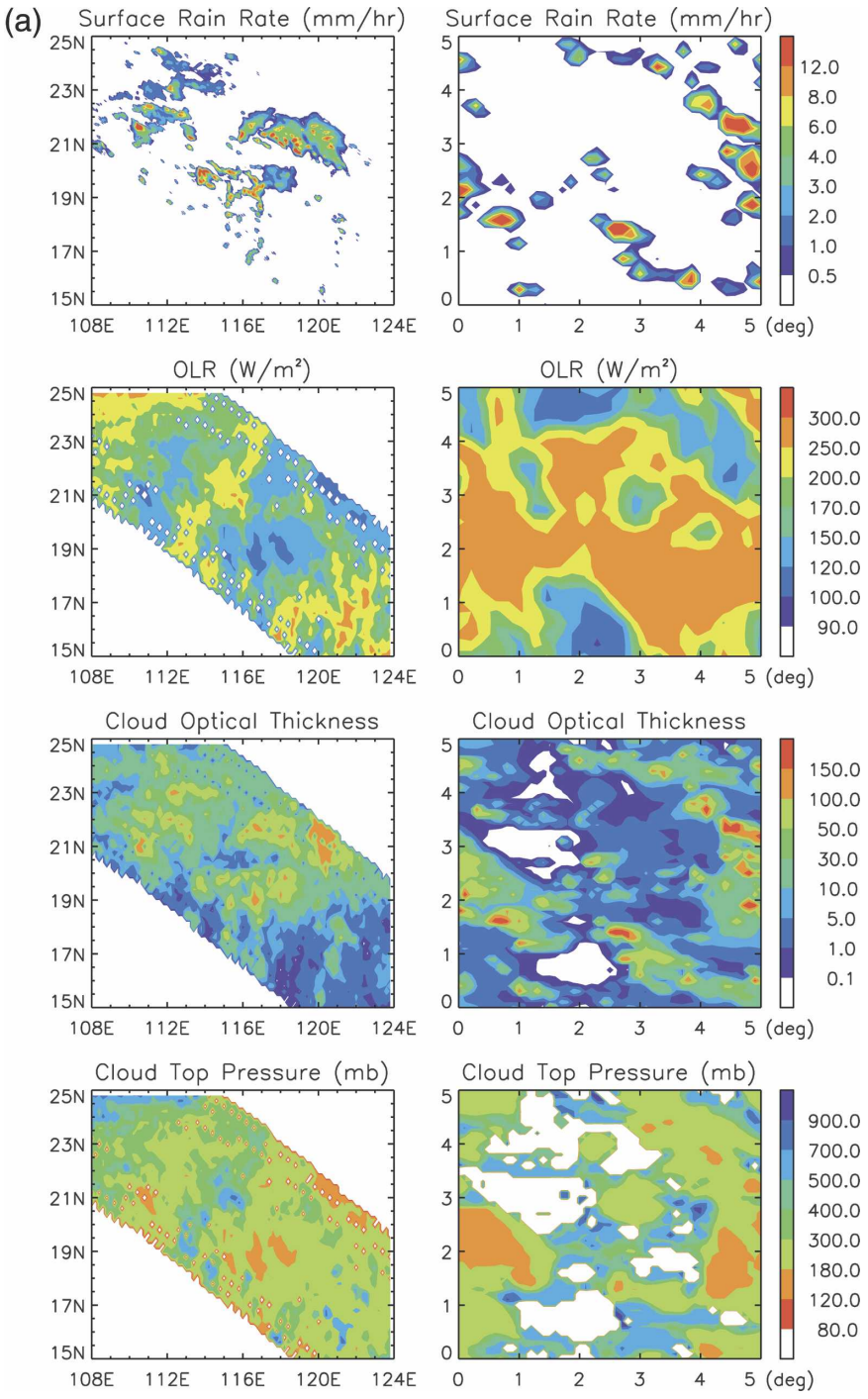

FIG. 2a. (left) Snapshot images of rain and cloud properties from TRMM satellite observations, coordinates are actual lat and lon; (right) corresponding GCE simulation, coordinates are approximate lengths (°) at 0800 UTC 19 May 1998.

model. The statistics suggest that the satellite observations collected over the specified month-long period also provide a sufficient sample to represent the cloud and rain systems over the period. However, we will use all of the GCE data (not just the data corresponding to satellite overpasses) to obtain more robust statistics for assessing GCE performance in the rest of this paper.

Table 3 shows that about 11.8% of the area of the

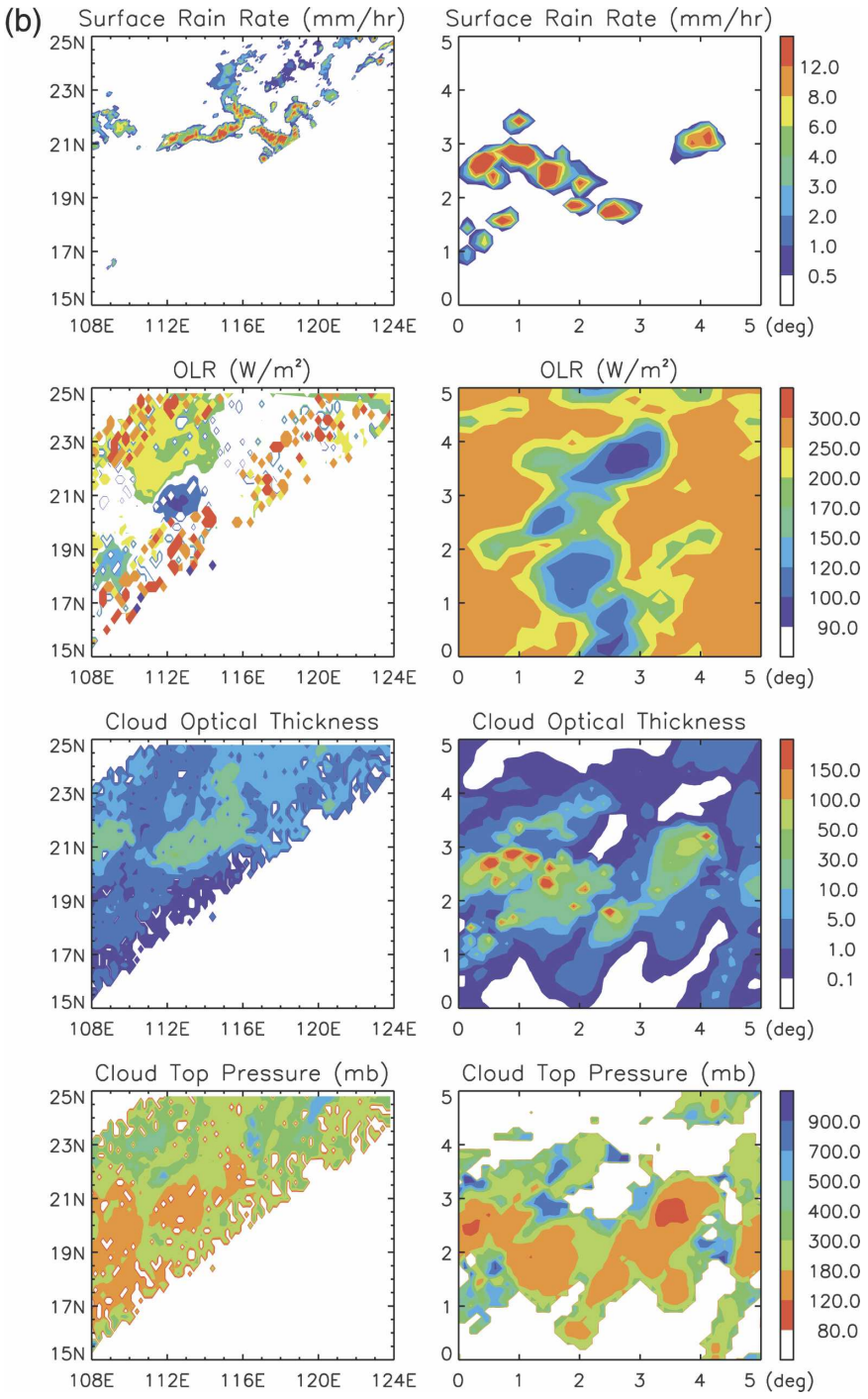

FIG. 2b. Same as in (a) but at 1600 UTC 4 Jun 1998.

GCE simulation has a rain rate smaller than 0.5 mm h^{-1} at 4-km resolution, compared to 1.97% from PR. At the coarser resolution of 14 km, 16.3% of the area of the GCE simulation has a rain rate smaller than 0.5 mm h^{-1}, compared to 4.75% from TMI. Since PR only senses precipitation down to 18 dBZ, or 0.3 mm h^{-1}, and since TMI has difficulty discriminating rain from cloud in light rain conditions, it is not conclusive whether the much larger percentage of rain area simulated by GCE relative to observations in the light rain range is due to excessive "drizzle" in the model or undetected light rain in the observations. Both PR and

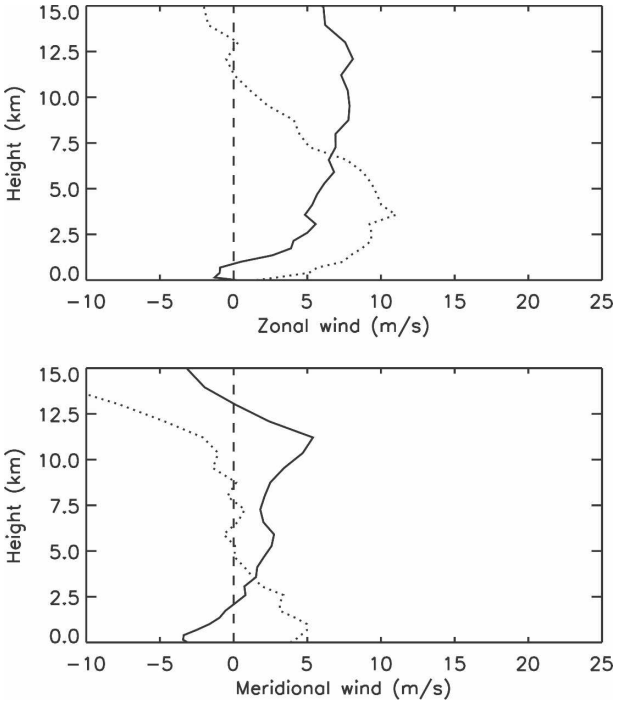

FIG. 3. Domain-averaged (a) horizontal and (b) meridional wind component at 0800 UTC 19 May (solid line) and 1600 UTC 4 Jun (dotted line).

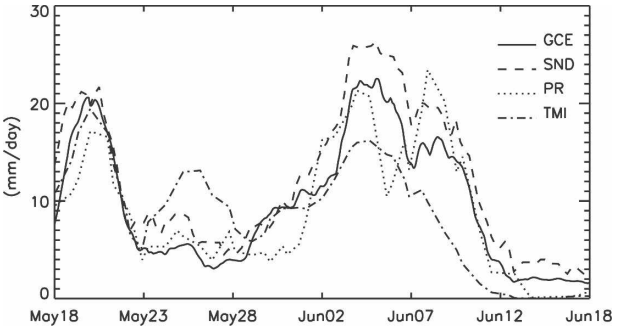

FIG. 4. Domain-averaged precipitation from GCE simulation vs estimates from sounding, TMI, and PR instruments.

TMI have higher percentages of rainy pixels in the intermediate rain range from 0.5 to 10 mm h^{-1}, and then the model has higher percentage of rainy pixels for heavier rains (a rain rate greater than 10 mm h^{-1}). Figure 5 shows the PDF of total rain amount contributed by different rain intensities. The bin interval of the PDF is 1 mm h^{-1} and the cutoff threshold is 0.5 mm h^{-1}, for the reasons discussed above. The PDFs of the GCE simulation are much flatter than those of the TMI and PR, although there are only small differences in the percentages of rainy pixels (>0.5 mm h^{-1}) as shown in Table 3. This figure indicates that more precipitation simulated by GCE comes from heavier rains compared to what PR or TMI observe. The PDF of TMI rainfall amount shows a unique peak contribution at around 4 mm h^{-1} and a decreasing contribution from rain rates smaller than 4 mm h^{-1}. The PDF also decreases much faster at heavy rain rates with very little contribution from rain rates greater than 25 mm h^{-1}. One reason for this distribution is the smoothing effect of the Bayesian technique, which, faced with the reduced sensitivity of microwave brightness temperatures to rain rate at high and low rain rates, tends to reduce the dynamic range of the rain estimates. It was found that the TMI version 6 algorithm has high (low) bias for low (high) retrieved rain rate (Olson et al. 2006). These positive and negative biases might have contributed to the peak rain value around 4 mm h^{-1} and the rapid decline of the PDF beyond 10 mm h^{-1}. Since the large percentage of low rain rates in the GCE simulation might bias the rain statistics, in the following, the rain statistics include only rain pixels with rain rate >0.5 mm h^{-1}, aside from the analysis of domain-averaged quantities.

c. Convective, stratiform rain

The partition of convective and stratiform rain in GCE- and satellite-based techniques have some similarity but are based on different algorithms as introduced in section 3, so that comparisons of relative contributions of total rainfall from convective and stratiform rain is qualitative at best.

From Table 2, it may be noted that the GCE produces a larger percentage of convective rain during the 2–11 June period than the 18–26 May period. PR and TMI show less variation in these two periods. On average, 63% of the total rainfall in GCE is due to con-

TABLE 2. Domain-averaged surface rainfall (mm day^{-1}), convective rainfall, and rain area in percentage from GCE simulation as well as estimated from TRMM PR, TMI, and sounding network.

Period	GCE-3D rainfall/convective rainfall/convective rain area	Sounding rainfall	PR rainfall/convective rainfall/convective rain area	TMI rainfall/ convective rainfall
18–26 May	9.9/55/17	13.0	9.2/54/20	11.0/71
2–11 Jun	15.5/67/20	20.7	15.8/56/21	9.6/72
18 May–18 Jun	10.2/63/20	12.3	9.2/56/22	8.3/59

TABLE 3. Rain statistics (percentage of rainy pixels) from GCE simulation, TMI, and PR measurements for 18 May–18 Jun 1998. The GCE simulated rainfall is integrated into 4- and 14-km resolutions to be comparable with PR and TMI observations, respectively.

Rain pixel (%)	GCE overpass (4 km)	GCE overpass (14 km)	GCE all data (4 km)	GCE all data (14 km)	PR (4 km)	TMI (14 km)
0.0–0.5 mm h^{-1}	10.3%	14.5%	11.8%	16.3%	1.97%	4.75%
0.5–2 mm h^{-1}	1.93%	2.66%	2.10%	2.81%	4.09%	2.86%
2–10 mm h^{-1}	1.86%	2.57%	1.88%	2.68%	3.17%	3.75%
10–25 mm h^{-1}	0.62%	0.82%	0.67%	0.94%	0.64%	0.83%
25–50 mm h^{-1}	0.25%	0.22%	0.30%	0.25%	0.19%	0.01%
>50 mm h^{-1}	0.10%	0.03%	0.12%	0.03%	0.05%	0.0%

vective rain, this is about 13% and 6% higher than PR and TMI, respectively. The percentage of convective rain area versus total rain area is around 20% for GCE, which seems not to vary too much for the two periods and is also quite close to PR observations. Presented in Fig. 6 are time series of the ratios of domain-averaged convective rainfall versus total rainfall. There is quite large variation of instantaneous convective/total rainfall ratio from both TMI and PR. The convective ratio from GCE varies in the neighborhood of 0.6 most of the time. It increases to a value close to 100% around 23 and 27 May, at which times there is very little rain. The only time the percentage of convective raindrops below 0.3 is during 24 May, which implies domination of stratiform precipitation.

d. Hydrometeor profiles

The TMI algorithm retrieves vertical structure of hydrometeor profiles in four forms (cloud liquid water, cloud ice water, precipitation water, and precipitation ice). However, cloud liquid and cloud ice from TMI are not very reliable estimates, since they are only "retrieved" by correlations with the precipitation water amounts, and the correlations are derived from GCE itself. Liquid- and ice-phase precipitation produce different microwave signatures in TMI data over ocean, and therefore we can compare these with the GCE simulation. The time–altitude cross sections of domain-averaged precipitation water and ice are shown for TMI (Fig. 7, left) and GCE (Fig. 7, right). It can be seen that the GCE simulation generally follows the vertical structure and time variations of the TMI retrieval, but the model produces heavier precipitation water (rain) and ice (mainly contributed by the graupel amount). There is a sharp transition between rain and ice at the freezing level (approximately 5 km) from GCE. The TMI retrievals show a gradual transition zone that extends from 2 to 6 km. The precipitation ice in TMI also extends higher than that of the GCE simulation to an altitude of about 16 km, while precipitation ice in GCE is limited to below 14 km. These reflect the fact that TMI profiles are a "composite" of many possible profiles as constrained by the observed radiances, so that profiles from a broader spectrum might have contaminated the retrieved profiles. Since TMI only retrieves vertical profiles for rainy pixels, we also computed domain averages of GCE profiles from rainy pixels only (figures not shown). The differences between domain-averaged profiles from all pixels and rainy-only pixels are very small, indicating that nonprecipitating cloud

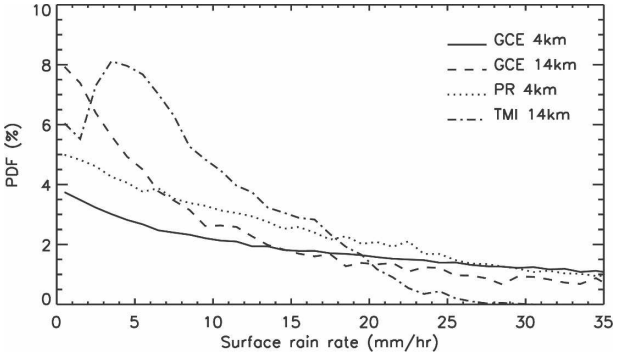

FIG. 5. Normalized PDF of total surface rain amount from GCE simulation and TMI and PR measurements from 18 May–18 Jun. The bin size is 1 mm h^{-1}, and minimum surface rain rate is 0.5 mm h^{-1}.

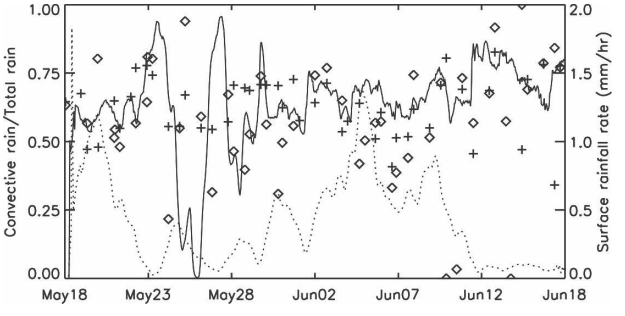

FIG. 6. Ratio of domain-averaged convective rainfall vs total rainfall from 18 May to 18 Jun from GCE simulation (solid line), TMI (+), and PR (◇). GCE-simulated total surface rainfall is plotted as the dotted line.

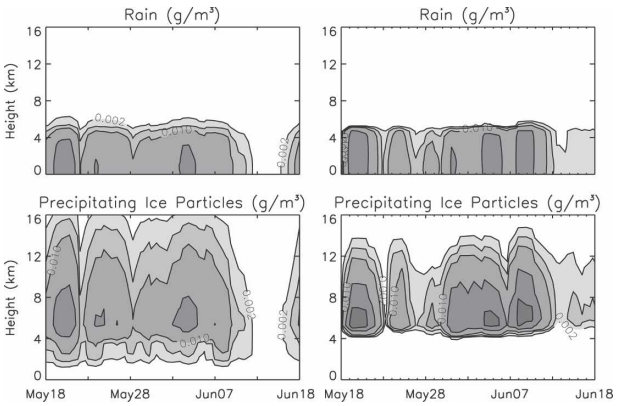

FIG. 7. Time–altitude cross sections of domain-averaged hydrometeor profiles from (left) TMI and (right) GCE simulation from 18 May to 18 Jun.

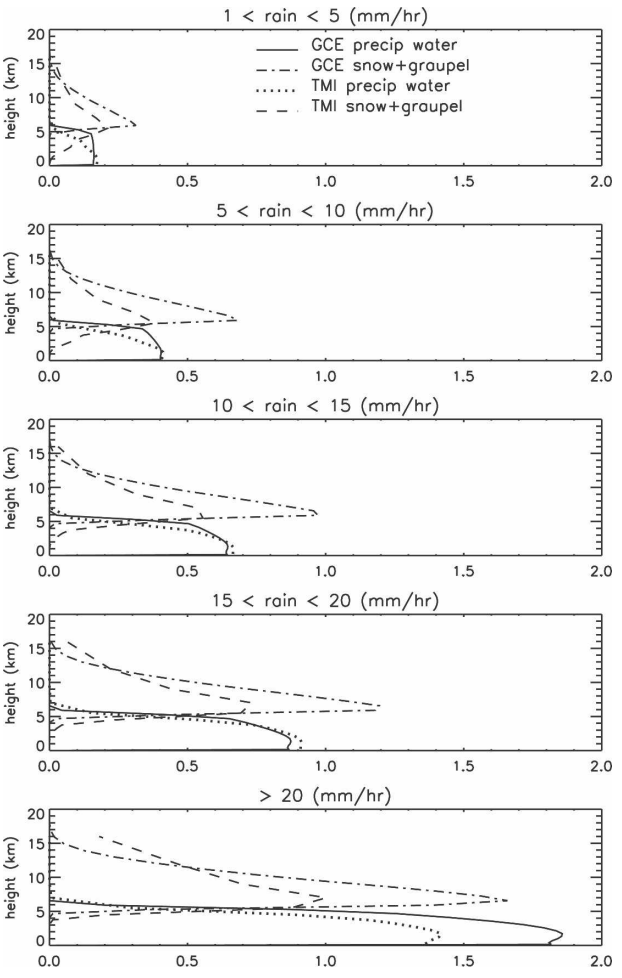

FIG. 8. Mean hydrometeor profiles from TMI and GCE for different rain ranges.

area does not contain a significant amount of precipitating particles in the atmosphere.

In addition to domain-averaged profiles, it is interesting to compare vertical profiles for specific rain intensities. Shown in Fig. 8 are TMI and GCE mean precipitation profiles corresponding to five rain-rate bins. While the GCE and TMI profiles have similar basic vertical structures, the discrepancies between the model and TMI are also quite obvious: for each rain-rate bin less than 20 mm h^{-1}, the GCE model's snow plus graupel amount is much greater than the estimated mean from the TMI retrieval. The precipitation water near the surface is relatively close to the TMI estimates, but the model shows a slower decrease with height below 5 km and a fast drop to zero above 5 km. Both the TMI and the model's precipitation ice content peak at 7 km, but TMI extends higher for heavier rains (>20 mm h^{-1}) and lower for light rains (<10 mm h^{-1}). Since the TMI retrievals are partially based on GCE simulations, the difference between the model profiles and TMI profiles for the same rain rate points out potential problems in the retrieval algorithm, and a possible bias in the model physics. Recently Grecu and Olson (2006) tested an algorithm similar to the TMI version 6 algorithm but used a PR/TMI-derived "empirical" database instead of CRM-generated database to derive surface rain rates and hydrometeor profiles. The new algorithm yields even lower mean precipitation water contents at upper levels than the version 6 algorithm. This confirms that the model does likely have too much upper-level snow and graupel.

Since GCE and TMI version 6 retrievals are not independent, the PR-observed rain profile is used to provide more insight. Direct comparisons between GCE and PR rain profiles cannot be made because the model outputs rainwater contents while the PR yields an equivalent rainfall rate. One way to compare GCE and PR is to convert the GCE hydrometeor profiles into equivalent radar reflectivity (Z) using the methods of Smith et al. (1975) and Smith (1984). The radar echo-top (Etop) height, which represents the maximum altitude of precipitation-size particles, can also be compared from GCE and PR. By comparing Z, there is no ambiguity due to assumptions made in retrieval algorithms.

Shown in Fig. 9 are the contoured cumulative frequencies by altitude diagrams (CCFAD) for the model-simulated and observed reflectivity stratified by convective and stratiform rains, respectively. The CCFAD is a modification of the cumulative frequencies by altitude diagrams (CFAD) used by Yuter and Houze (1995) and adopted by Eitzen and Xu (2005). The CCFAD uses a 2-dBZ bin size and a minimum of 18 dBZ because PR's minimum detectable reflectivity is 17 dBZ according to Fisher (2004). As seen in the fig-

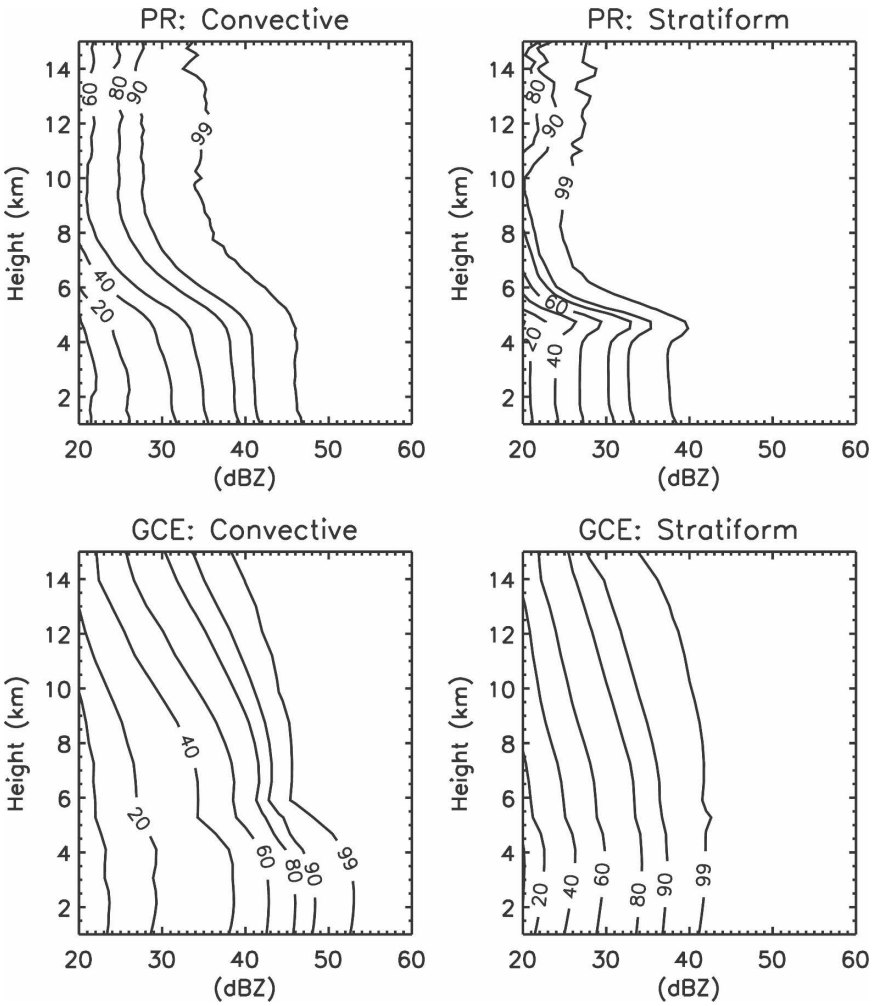

FIG. 9. Cumulative frequency distributions with altitude for radar reflectivity from PR (top left) convective and (top right) stratiform, and GCE simulation (bottom left) convective, and (bottom right) stratiform rain types. The bin size is 2 dBZ and minimum reflectivity is 18 dBZ.

ure, the CCFADs of convective and stratiform radar reflectivity from PR are significantly different from each other. The contours of cumulative PDF of PR's stratiform rain show a distinct bright band at 5 km and a sharp decrease in reflectivity above. Further inspection of the CCFADs of PR's stratiform rain with a bright band and without a bright band reveal that rain associated with a bright band produces much larger radar reflectivity below the freezing level than rain without a bright band (Fig. 10); therefore the bright band (or melting/freezing process) is responsible for the unique reflectivity structure seen in the CCFAD of stratiform rain. The radar reflectivity for the convective rain is generally larger than that of stratiform rain so that the contour shifts to larger values for convective rains observed by PR. The reflectivity of convective precipitation also decreases with altitude above the freezing level, especially for lighter rains ($Z < 30$ dBZ), but not as rapidly as it does for stratiform precipitation. The GCE seems to simulate the convective reflectivity relatively well, except that slightly greater reflectivity at lower altitudes and much larger reflectivity at higher altitudes are simulated, consistent with the previous analysis that the model tends to produce too much precipitation ice (Fig. 9). The GCE simulation misses the vertical structure and bright band in the stratiform rain completely. Bright band is formed when large falling snowflakes pass through a level where the temperature exceeds freezing and start to melt. The wet (water coated) snowflakes produce a higher reflectivity than dry snowflakes above. As the snowflakes continue to fall and melt, they collapse into raindrops. The raindrops are smaller and fall faster, so both the size of the particles and their concentration are reduced, reducing

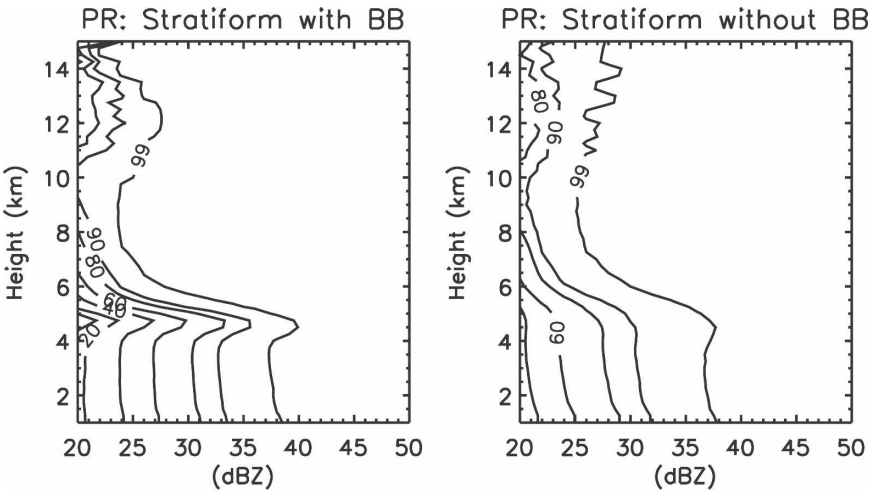

FIG. 10. Cumulative frequency distribution with altitude for radar reflectivity from PR stratiform rain (left) with bright band and (right) without bright band. The bin size is 2 dBZ and minimum reflectivity is 18 dBZ.

the radar reflectivity. This leads to the formation of a narrow band of high reflectivity near the melting level. Although the melting process is included in GCE, the GCE bulk microphysics scheme does not include explicit mixed-phase particles (only ice or liquid). In addition, the prescribed model vertical resolution through the melting layer may not be sufficient to resolve the narrow band of high reflectivity associated with melting. Therefore it is not possible to simulate a bright band using the output of GCE directly.

Presented in Fig. 11 are the PDFs of radar Etop from the PR and GCE simulation for stratiform, convective, and all rain conditions. From PR, the all-rain PDF of Etop resembles that of the stratiform rain with a substantial peak at 4–5 km. This is not surprising because the ice that melts to form weak stratiform rain has very low reflectivity; therefore, the echo top is roughly the freezing level. Also, stratiform rain covers a much larger area than convective rain (Table 2), and so the statistics are dominated by stratiform rains. The GCE simulation does not show a large peak at the melting level for stratiform rain because the model does not simulate bright band. It is also notable that the PR shows some evidence of a shallow convective mode; then a jump at 5 km that may be due to melting ice, even though there is no bright band, per se. There appear to be mainly two convective modes in the GCE simulation: shallow and very deep (extends to 10–15 km), while there is a significant population of intermediate-depth modes in the PR data. This indicates that model's vertical profiles of rain are still quite different from reality.

e. Cloud characteristics

Since the definition of a cloudy pixel is subject to arbitrary thresholds both in GCE and satellite observations, we will use cloud optical properties as well as

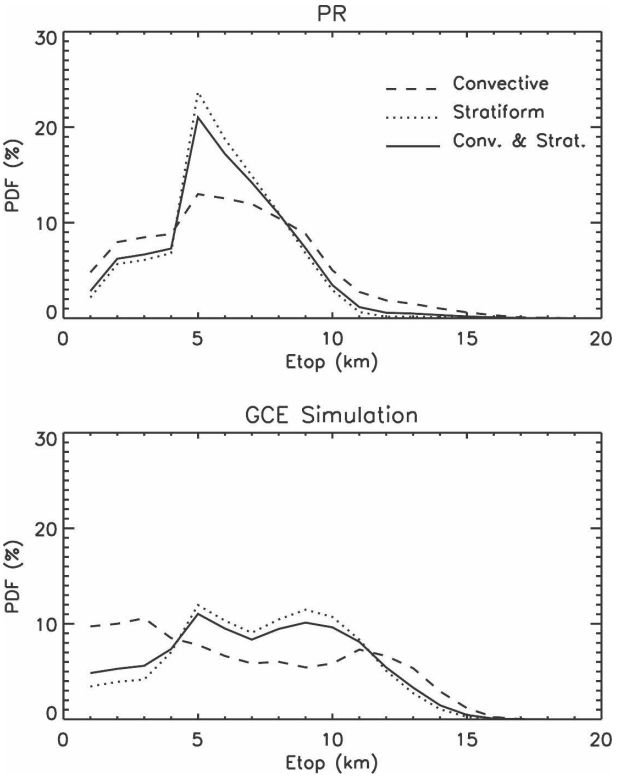

FIG. 11. PDF of radar Etop from (top) PR and (bottom) GCE simulation.

OLR and top-of-atmosphere (TOA) albedo to diagnose cloud characteristics from GCE and satellite observations, since OLR and albedo are not affected by the cloud threshold. Presented in Fig. 12 are the total cloud fraction, high cloud fraction (defined here as cloud top above 400 hPa), domain-averaged OLR, and TOA albedo from CERES and GCE. The CERES observations show that total cloud fraction is close to 100% during the deep convective episodes but drops to 50% and 40% in the intermediate quiescent periods around 23 May and 12 June, respectively. The drop of cloud fraction corresponds to the warming and drying of large-scale forcing presented in Fig. 1 around 23 May and 12 June. The mean cloud percentage from CERES for the period is 78% and the mean high cloud percentage is 50%. Two methods have been used to define a cloud grid for GCE output in this study: the cloud mixing ratio threshold and optical thickness threshold. When using mixing ratio threshold, higher cloud thresholds result in smaller cloud fractions except around 24–25 May when all methods yield close to 100% cloud fraction. The mean cloud percentages for the period are 64%, 57%, and 51% using total hydrometeor thresholds of 0.002, 0.005, and 0.008 g kg^{-1}, respectively. The corresponding mean high cloud percentages are 38%, 31%, and 27% using these thresholds. Using an optical thickness threshold of 0.3 results in 48% of total cloud fraction and 30% high cloud fraction, roughly comparable to the cloud fraction using total hydrometeor threshold of 0.005 g kg^{-1}. For the current case, it is obvious that the model does not produce enough cloud area using any of the chosen thresholds. The higher fraction of total cloud area from CERES is consistent with the lower domain-averaged OLR and higher TOA albedo relative to GCE seen during most of the period (Fig. 12).

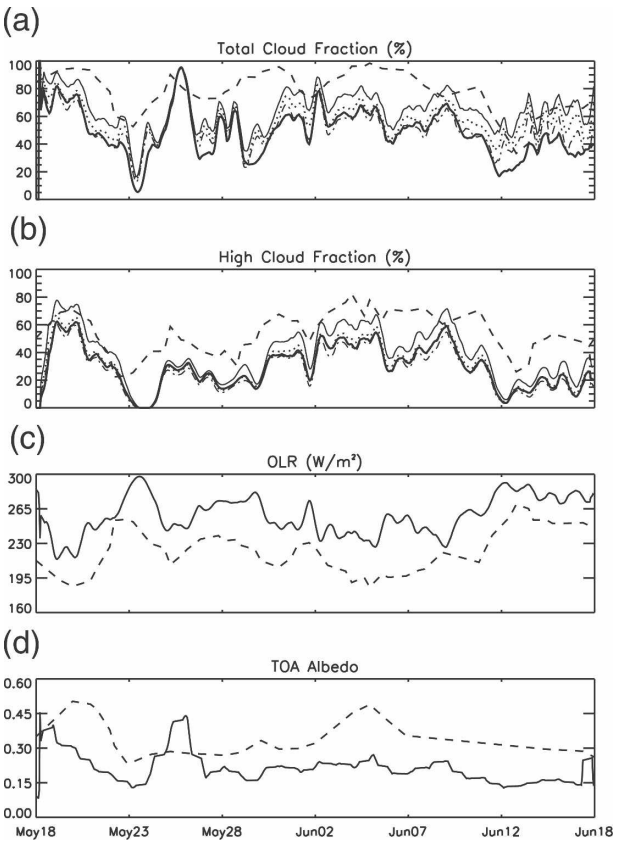

FIG. 12. Domain-averaged (a) total cloud fraction, (b) high cloud fraction, (c) OLR, and (d) TOA albedo from CERES measurements (dashed lines) and GCE simulation (solid lines) from 18 May to 18 Jun 1998. The GCE cloud fractions are defined using threshold of total hydrometeor density of 0.002 g kg^{-1} (thin solid line), 0.005 g kg^{-1} (dotted line), 0.008 g kg^{-1} (dash dotted line), and optical thickness of 0.3 (thick solid line).

To further examine the cloud populations within the domain, the PDFs of OLR, effective cloud-top pressure, and visible optical thickness from both the model and CERES are shown in Fig. 13. The GCE cloud properties are spatially averaged to 10-km resolution to be consistent with the definitions of the CERES SSF cloud products (although the CERES footprint size may be larger than 10 km with larger viewing angles). All the PDFs show asymmetric characteristics. The PDFs of OLR from CERES and GCE are both negatively skewed, with the GCE being more concave upward with a higher peak percentage around 290 W m^{-2} and a significantly smaller percentage of OLR that is less than 250 W m^{-2} (Fig. 13a). The PDF of OLR from CERES is much flatter and peaks at 270 W m^{-2}. This implies that the CERES observations are more continuous in observed cloud and clear field while the model is dominated with clear area but small sporadic high- and midlevel clouds. The PDFs of effective cloud top from CERES and GCE are both positively skewed toward high cloud top, with GCE being more concave upward (Fig. 13b). The PDF of CERES effective cloud top peaks at 230 hPa and gradually decreases toward high and low cloud (Fig. 13b). The effective cloud top from the GCE model has a peak frequency near 190 hPa but decreases much faster toward midlevel cloud than the CERES observations. Note that the PDFs of effective cloud top only include cloudy pixels so that the peak frequencies are shown for high clouds, while the PDFs of OLR include all pixels, so that peak frequencies are located for clear pixels. The model also shows small frequency peaks below 700 hPa that CERES does not observe. The higher cloud top from GCE may be due to updrafts that are too strong in the 3D model and the maximum height of the cloud-resolving model; see Lang et al. (2007). The PDFs of

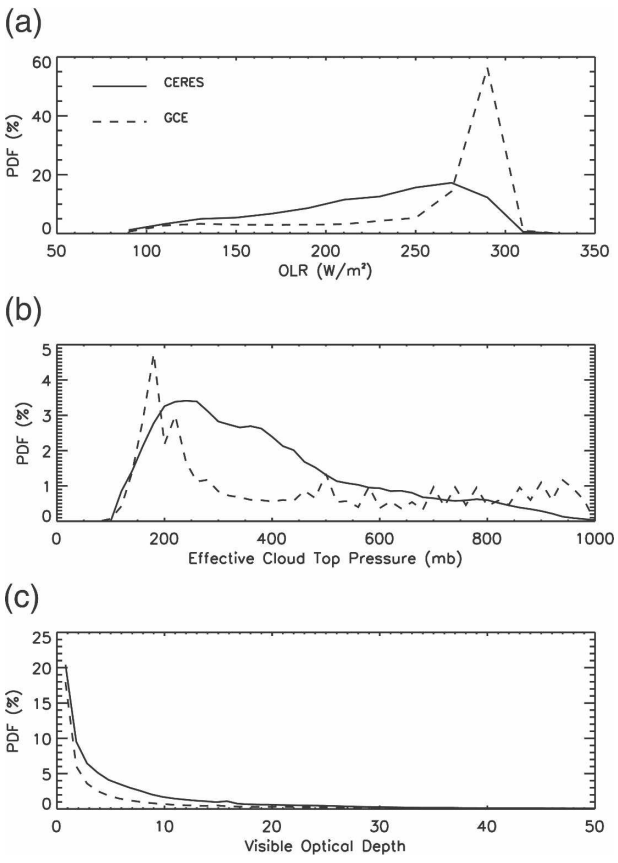

FIG. 13. The probability distribution functions of (a) OLR, (b) effective cloud-top pressure, and (c) visible optical thickness from CERES and GCE simulation. The bin size for OLR, effective cloud-top pressure, and optical thickness are 20 W m^{-2}, 20 hPa, and 1, respectively. The cutoff threshold for optical thickness is 0.3.

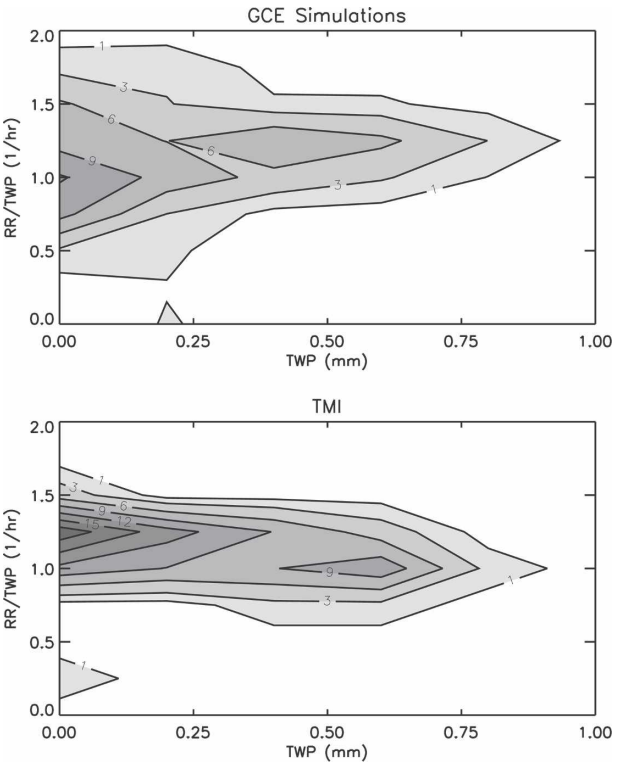

FIG. 14. 2D frequency distributions of precipitation efficiency (RR/TWP) vs total condensate (TWP) from (top) GCE and (bottom) TMI simulations. The bin size for precipitation efficiency and total condensed water is 0.25 and 0.2, respectively. The contour is normalized percentage.

optical depth for both the model and the CERES observations use a cutoff threshold of 0.3 because the CERES instrument cannot detect cloud when the optical thickness is less than 0.3 (Fig. 13c). The bin size is one for optical thickness. The PDFs of optical depth show exponential decreases of frequency with increasing optical depth, which means thin anvil clouds dominate deep convective clouds in terms of area. The GCE simulation generally shows a lower frequency of occurrence for this optical thickness range and is slightly more skewed toward small values than the PDF of the CERES data, which is consistent with the overall less cloud fraction as shown in Fig. 12.

f. Precipitation efficiency

Precipitation efficiency (PE) relates the amount of surface rainfall to the moisture influx or cloud condensation in a storm system, but the precise definition of precipitation efficiency varies in different modeling (Weisman and Klemp 1982; Lipps and Hemler 1986; Tao et al. 2004) and observational studies (Del Genio and Kovari 2002; Lau and Wu 2003; Lin et al. 2006). In this paper, we define the precipitation efficiency in two ways: for the whole storm using domain-averaged quantities and for individual grid locations to interpret the microphysical impact.

For the stormwide precipitation efficiency, we use the ratio of domain mean surface rain rate (RR) to the domain mean column condensate (TWP, including liquid- and ice-phase cloud and precipitation) from both TMI retrievals and GCE simulation. High precipitation and low condensate mean the system is more efficient in converting the condensate into surface rain. Presented in Fig. 14 are the 2D histograms of precipitation efficiency (RR/TWP) versus total condensate (TWP) based upon TMI retrievals and GCE simulation. Although rainfall retrieval from TMI for individual pixels might be less certain as discussed in section 4b, the ratio of domain-averaged rainfall and column condensate reflect the basic physical processes relating water condensate and rain. Both PDFs show two distribution modes:

one with high total condensation and one with low total condensation. The high total condensation mode is likely associated with large and heavy rain systems and low condensation mode is associated with small, light rain systems. The GCE model has a larger range of precipitation efficiency than TMI when the total condensation is low. The peak frequency of the model's PE is about 1.0, while TMI's peak frequency is around 1.25. The TMI shows slightly decreasing PE with increasing water load and the GCE has slightly increasing PE with increasing water load. This indicates that although the model is less efficient in small rains compared to TMI, it is increasingly more efficient in raining out in heavy rain events, likely resulting in less anvil cloud than that seen in the observations.

At the pixel level, we define a precipitation efficiency as the ratio of surface rain rate to the PR-integrated precipitation water (RR/precipWaterSum) since individual TMI profiles are less reliable at footprint scale. The TRMM PR can only detect rain signal, and so this analysis only reflects part of the physics involved, that is, the conversion of precipitation in the vertical column to the rain flux at the surface. The GCE vertically integrated precipitation water is calculated from rain, snow, and graupel amount in the vertical layer where the corresponding radar reflectivity is greater than 17 dBZ, so that it is consistent with PR measurements. Shown in Fig. 15 are mean precipitation efficiencies for each surface rain bin from 0.5 to 25 mm h^{-1} with bin size of 1 mm h^{-1} for both the PR and GCE. The upper panel shows that the mean precipitation efficiency of stratiform with bright band category is lower than either convective or stratiform without bright band categories from PR. The result means that the precipitation-sized condensate in the air falls out more slowly as surface rain when a bright band exists, because snow falls relatively slowly through the weak updrafts in stratiform regions before it melts and falls out as rain; that is, there is relatively more snow just above the freezing level, and it is only gradually being converted to rain. In convective regions, the raindrop collision/coalescence (warm rain) process is a fairly efficient producer of rain in the Tropics, more dense graupel particles aloft fall faster, and raindrops/graupel are aided by stronger downdrafts to produce rain more quickly at the surface. The middle panel shows convective and stratiform rain categories for the GCE simulation. The GCE model has much higher precipitation efficiency for convective rain than stratiform rain for rain rates less than 20 mm h^{-1}. This is because GCE has an excessive snow and graupel amount above the freezing level for stratiform rain as shown in Fig. 8. There is a

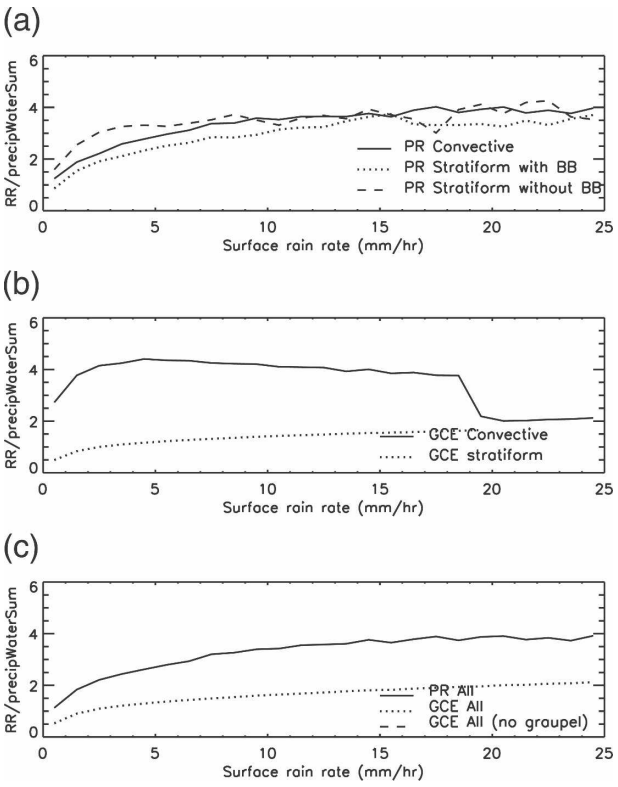

FIG. 15. Mean PEs (RR/precipWaterSum) binned for surface rain rate from GCE and PR retrievals. PEs stratified for (a) convective, stratiform with bright band, and stratiform without brightband categories from PR; (b) convective and stratiform rain from GCE; (c) all cases from PR and GCE. The bin size of surface rain rate is 1 mm h^{-1}.

discontinuity of the model's convective and stratiform curves at approximately 20 mm h^{-1} because of the specified threshold in the model to separate convective and stratiform rain. The lower panel compares mean precipitation efficiencies from PR and GCE for all rain cases. It may be noted that, for the same surface rain rate, the model yields lower mean precipitation efficiency than PR because of its high graupel amount for stratiform rain. If graupel is excluded, the model has slightly higher precipitation efficiency than PR. Combining the results from Figs. 14 and 15, it seems that the model is quite efficient in convective and heavy rain situations but less efficient in converting graupel into rain in stratiform rain conditions.

5. Summary

In this paper, the cloud and precipitation statistics simulated using the 3D GCE cloud-resolving model over SCSMEX during 18 May–18 June 1998 are com-

pared with TRMM TMI and PR rainfall measurements and CERES single scanner footprint radiation and cloud retrievals. The aggregate effect of cloud and rain systems are considered by systematically examining important parameters such as surface rain rate, convective/stratiform percentage, rain profiles, OLR, cloud optical properties, and precipitation efficiency.

The study shows that the model captures the time evolution and major features of convective systems quite well. It reproduces organized mesoscale convective systems with orientations similar to observations when the environmental wind shear is strong but less organized small (but intense) precipitation cells when the environmental wind shear is weak.

Consistent with many previous studies (Grabowski et al. 1998; Khairoutdinov and Randall 2003; Xie et al. 2005; Xu et al. 2005; Zeng et al. 2007), this study shows that GCE is capable of reproducing the total rain amount as compared to rainfall estimated from sounding data. The GCE rainfall spectrum includes a greater proportion of heavy rains than PR or TMI observations. TMI seems to underestimate the high rain rates because of the lack of sensitivity of radiances and the smoothing effect of the Bayesian technique.

The GCE model produces excessive condensed water loading in the column, especially the amount of graupel as indicated by both TMI and PR observations, and reported by other studies (Lang et al. 2007; Zeng et al. 2007). The model also cannot simulate the bright band and the sharp decrease of radar reflectivity above the freezing level in stratiform rain as seen from PR. The lack of a bright band is due to the simplified bulk microphysics scheme used in the GCE simulation (Olson et al. 1996).

Comparing GCE-simulated OLR, cloud optical thickness and effective cloud top to CERES measurements, it is found that the model has much higher domain-averaged OLR due to smaller total cloud fraction, a result contrary to the ARM/SGP site simulation by Zeng et al. (2007). The PDFs of OLR and effective cloud top from GCE show that the model has a more skewed distribution of OLR and effective cloud top than CERES observations, indicating that the model's cloud field is insufficient in area extent.

The precipitation efficiency is examined for the whole storm using domain-averaged quantities, as well as at pixel level to examine the microphysical processes. The domain-averaged precipitation efficiency from GCE is very close to that derived from TMI because GCE generates both heavier rain and more condensed water than TMI. The GCE is quite efficient in convective or heavy rain conditions while not very efficient in stratiform rain conditions because of the large amounts of slowly falling snow and graupel that are simulated.

The analysis demonstrates that the GCE model is quite robust in reproducing the total surface rain, rain variation with time, and the convective/stratiform rain partition. Large differences between model and observations exist in the rain spectrum and the vertical hydrometeor profiles that contribute to the associated cloud field. The GCE model seems to yield slightly lower overall precipitation efficiency than that derived from TRMM observations. It tends to produce more intense convection and less anvil cloud.

The discrepancies between the GCE simulation and satellite observations can be contributed to many factors including uncertainties in measurements and imperfect model physics. Accurate and consistent large-scale advective tendencies of temperature and water vapor are also crucial for the GCE simulation. In Part II, sensitivity tests will be conducted to evaluate the impact of model setup (i.e., model resolution, domain size, etc.) and various microphysics schemes on the rain spectrum and vertical hydrometeor profiles. Analyses of other case studies will be needed in order to establish the generality of the results from this study and to determine how the differences between model-simulated and observed parameters vary with environmental conditions.

Acknowledgments. This work is mainly sponsored by NASA Interdisciplinary Research in Earth Science NRA-02-OES-06. Support of this research by the NASA Earth Science Enterprise's Multidisciplinary Research in Climate, Chemistry, and Global Modeling under WBS 509496.02.01.01.07, UPN 291-01-97-05, and UPN 291-01-c7 is gratefully acknowledged. The authors thank anonymous reviewers for their thoughtful comments and suggestions that helped improve the manuscript. The TRMM and CERES data were obtained from Goddard Earth Sciences Distributed Active Archive Center and the Atmospheric Sciences Data Center at the NASA Langley Research Center, respectively.

REFERENCES

Alexander, G. D., and G. S. Young, 1992: The relationship between EMEX mesoscale precipitation feature properties and their environmental characteristics. *Mon. Wea. Rev.,* **120,** 554–564.

Awaka, J., T. Iguchi, and K. Okamoto, 1998: Early results on rain type classification by the Tropical Rainfall Measuring Mission (TRMM) precipitation radar. *Proc. Eighth URSI Commission F Open Symp.,* Aveiro, Portugal, Union Radio-Scientifigue Internationale, 143–146.

Caniaux, G., J.-L. Redelsperger, and J.-P. Lafore, 1994: A numeri-

cal study of the stratiform region of a fast-moving squall line. Part I: General description and water and heat budgets. *J. Atmos. Sci.,* **51,** 2046–2074.

Churchill, D. D., and R. A. Houze Jr., 1984: Development and structure of winter monsoon cloud clusters on 10 December 1978. *J. Atmos. Sci.,* **41,** 933–960.

Del Genio, A. D., and W. Kovari, 2002: Climatic properties of tropical precipitating convection under varying environmental conditions. *J. Climate,* **15,** 2597–2615.

Donner, L. J., C. J. Seman, and R. S. Hemler, 1999: Three-dimensional cloud-system modeling of GATE convection. *J. Atmos. Sci.,* **56,** 1885–1912.

Dudhia, J., M. W. Moncrieff, and D. W. K. So, 1987: The two-dimensional dynamics of West African squall lines. *Quart. J. Roy. Meteor. Soc.,* **113,** 121–146.

Eitzen, Z. A., and K.-M. Xu, 2005: A statistical comparison of deep convective cloud objects observed by an Earth Observing System satellite and simulated by a cloud resolving model. *J. Geophys. Res.,* **110,** D15S14, doi:10.1029/2004JD005086.

Fairall, C., E. F. Bradley, D. P. Rogers, J. B. Edson, and G. S. Young, 1996: Bulk parameterization of air–sea fluxes for TOGA COARE. *J. Geophys. Res.,* **101,** 3747–3764.

Fisher, B. L., 2004: Climatological validation of TRMM TMI and PR monthly rain products over Oklahoma. *J. Appl. Meteor.,* **43,** 519–535.

Grabowski, W. W., X. Wu, and M. W. Moncrieff, 1996: Cloud-resolving modeling of tropical cloud systems during phase III of GATE. Part I: Two-dimensional experiments. *J. Atmos. Sci.,* **53,** 3684–3709.

——, ——, ——, and W. D. Hall, 1998: Cloud-resolving modeling of cloud systems during phase III of GATE. Part II: Effects of resolution and the third spatial dimension. *J. Atmos. Sci.,* **55,** 3264–3282.

Grecu, M., and W. S. Olson, 2006: Bayesian estimation of precipitation from satellite passive microwave observations using combined radar–radiometer retrievals. *J. Appl. Meteor. Climatol.,* **45,** 416–433.

Hong, Y., C. D. Kummerow, and W. S. Olson, 1999: Separation of convective and stratiform precipitation using microwave brightness temperature. *J. Appl. Meteor.,* **38,** 1195–1213.

Johnson, D., W.-K. Tao, J. Simpson, and C.-H. Sui, 2002: A study of the response of deep tropical clouds to large-scale thermodynamic forcings. Part I: Modeling strategies and simulations of TOGA COARE convective systems. *J. Atmos. Sci.,* **59,** 3492–3518.

Johnson, R. H., and P. E. Ciesielski, 2002: Characteristics of the 1998 summer monsoon onset over the northern South China Sea. *J. Meteor. Soc. Japan,* **80,** 561–578.

——, S. L. Aves, P. E. Ciesielski, and T. D. Keenan, 2005: Organization of oceanic convection during the onset of the 1998 East Asian summer monsoon. *Mon. Wea. Rev.,* **133,** 131–148.

Keenan, T. D., and R. E. Carbone, 1992: A preliminary morphology of precipitation systems in tropical northern Australia. *Quart. J. Roy. Meteor. Soc.,* **118,** 283–326.

Khairoutdinov, M. F., and D. A. Randall, 2003: Cloud resolving modeling of the ARM summer 1997 IOP: Model formulation, results, uncertainties, and sensitivities. *J. Atmos. Sci.,* **60,** 607–625.

——, ——, and C. DeMott, 2005: Simulations of the atmospheric general circulation using a cloud-resolving model as a super-parameterization of physical processes. *J. Atmos. Sci.,* **62,** 2136–2154.

Klemp, J. B., and R. Wilhelmson, 1978: The simulation of three-dimensional convective storm dynamics. *J. Atmos. Sci.,* **35,** 1070–1096.

Krueger, S. K., 1988: Numerical simulation of tropical cumulus clouds and their interaction with the subcloud layer. *J. Atmos. Sci.,* **45,** 2221–2250.

Kummerow, C., W. Barnes, T. Kozu, J. Shiue, and J. Simpson, 1998: The Tropical Rainfall Measuring Mission (TRMM) sensor package. *J. Atmos. Oceanic Technol.,* **15,** 809–817.

——, and Coauthors, 2001: The evolution of the Goddard Profiling Algorithm (GPROF) for rainfall estimation from passive microwave sensors. *J. Appl. Meteor.,* **40,** 1801–1820.

Lang, S., W.-K. Tao, J. Simpson, and B. Ferrier, 2003: Modeling of convective–stratiform precipitation processes: Sensitivity to partitioning methods. *J. Appl. Meteor.,* **42,** 505–527.

——, ——, R. Cifelli, W. Olson, J. Halverson, S. Rutledge, and J. Simpson, 2007: Improving simulations of convective systems from TRMM LBA: Easterly and westerly regimes. *J. Atmos. Sci.,* **64,** 1141–1164.

Lau, K. M., and H. T. Wu, 2003: Warm rain processes over tropical oceans and climate implications. *Geophys. Res. Lett.,* **30,** 2290, doi:10.1029/2003GL018567.

——, and Coauthors, 2000: A report of the field operations and early results of the South China Sea Monsoon Experiment (SCSMEX). *Bull. Amer. Meteor. Soc.,* **81,** 1261–1270.

LeMone, M. A., E. J. Zipser, and S. B. Trier, 1998: The role of environmental shear and thermodynamic conditions in determining the structure and evolution of mesoscale convective systems during TOGA COARE. *J. Atmos. Sci.,* **55,** 3493–3518.

Li, X., C.-H. Sui, and K.-M. Lau, 2002: Interactions between tropical convection and its environment: An energetics analysis of a 2D cloud resolving simulation. *J. Atmos. Sci.,* **59,** 1712–1722.

Lin, B., B. A. Wielicki, P. Minnis, L. Chambers, K.-M. Xu, Y. Hu, and A. Fan, 2006: The effect of environmental conditions on tropical deep convective systems observed from the TRMM satellite. *J. Climate,* **19,** 5745–5761.

Lin, Y.-L., R. D. Farley, and H. D. Orville, 1983: Bulk parameterization of the snow field in a cloud model. *J. Appl. Meteor.,* **22,** 1065–1092.

Lipps, F. B., and R. S. Hemler, 1986: Numerical simulation of deep tropical convection associated with large-scale convergence. *J. Atmos. Sci.,* **43,** 1796–1816.

Loeb, N. G., N. Manalo-Smith, S. Kato, W. F. Miller, S. K. Gupta, P. Minnis, and B. A. Wielicki, 2003: Angular distribution models for top-of-atmosphere radiative flux estimation from the Clouds and the Earth's Radiant Energy System instrument on the Tropical Rainfall Measuring Mission satellite. Part I: Methodology. *J. Appl. Meteor.,* **42,** 240–265.

Minnis, P., and Coauthors, 1997: Cloud optical property retrieval (Subsystem 4.3). Clouds and the Earth's Radiant Energy System (CERES) algorithm theoretical basis document. Vol. III: Cloud analyses and radiance inversions (Subsystem 4), CERES Science Team, Eds., NASA, 60 pp. [Available online at http://asd-www.larc.nasa.gov/ATBD/ATBD.html.]

Moncrieff, M. W., and J. S. A. Green, 1972: The propagation and transfer properties of steady convective overturning in shear. *Quart. J. Roy. Meteor. Soc.,* **98,** 336–352.

——, S. K. Krueger, D. Gregory, J.-L. Redelsperger, and W.-K.

Tao, 1997: GEWEX Cloud System Study (GCSS) Working Group 4: Precipitating convective cloud systems. *Bull. Amer. Meteor. Soc.,* **78,** 831–845.

Olson, W. S., C. D. Kummerow, G. M. Heymsfield, and L. Giglio, 1996: A method for combined passive–active microwave retrievals of cloud and precipitation profiles. *J. Appl. Meteor.,* **35,** 1763–1789.

——, Y. Hong, C. D. Kummerow, and J. Turk, 2001: A texture-polarization method for estimating convective–stratiform precipitation area coverage from passive microwave radiometer data. *J. Appl. Meteor.,* **40,** 1577–1591.

——, and Coauthors, 2006: Precipitation and latent heating distributions from satellite passive microwave radiometry. Part I: Improved method and uncertainties. *J. Appl. Meteor. Climatol.,* **45,** 702–720.

Parker, M. D., and R. H. Johnson, 2004: Structures and dynamics of quasi-2D mesoscale convective systems. *J. Atmos. Sci.,* **61,** 545–567.

Petch, J. C., and M. E. B. Gray, 2001: Sensitivity studies using a cloud-resolving model simulation of the tropical west Pacific. *Quart. J. Roy. Meteor. Soc.,* **127,** 2287–2306.

Randall, D. A., K.-M. Xu, R. J. C. Somerville, and S. Iacobellis, 1996: Single-column models and cloud ensemble models as links between observations and climate models. *J. Climate,* **9,** 1683–1697.

——, M. Khairoutdinov, A. Arakawa, and W. Grabowski, 2003: Breaking the cloud parameterization deadlock. *Bull. Amer. Meteor. Soc.,* **84,** 1547–1564.

Rutledge, S. A., and P. V. Hobbs, 1984: The mesoscale and microscale structure and organization of clouds and precipitation in midlatitude cyclones. XII: A diagnostic modeling study of precipitation development in narrow cold-frontal rainbands. *J. Atmos. Sci.,* **41,** 2949–2972.

Shie, C.-L., W.-K. Tao, J. Simpson, and C.-H. Sui, 2003: Quasi-equilibrium states in the Tropics simulated by a cloud-resolving model. Part I: Specific features and budget analysis. *J. Climate,* **16,** 817–833.

Simpson, J., R. F. Adler, and G. R. North, 1988: A proposed Tropical Rainfall Measuring Mission (TRMM) satellite. *Bull. Amer. Meteor. Soc.,* **69,** 278–295.

——, C. Kummerow, W.-K. Tao, and R. Adler, 1996: On the Tropical Rainfall Measuring Mission (TRMM). *Meteor. Atmos. Phys.,* **60,** 19–36.

Skamarock, W. C., M. L. Weisman, and J. B. Klemp, 1994: Three-dimensional evolution of simulated long-lived squall lines. *J. Atmos. Sci.,* **51,** 2563–2584.

Smith, P. L., Jr., 1984: Equivalent radar reflectivity factors for snow and ice particles. *J. Climate Appl. Meteor.,* **23,** 1258–1260.

——, C. G. Myers, and H. D. Orville, 1975: Radar reflectivity factor calculations in numerical cloud models using bulk parameterization of precipitation. *J. Appl. Meteor.,* **14,** 1156–1165.

Smolarkiewicz, P. K., and W. W. Grabowski, 1990: The multidimensional positive definite advection transport algorithm: Nonoscillatory option. *J. Comput. Phys.,* **86,** 355–375.

Soong, S.-T., and Y. Ogura, 1980: Response of tradewind cumuli to large-scale processes. *J. Atmos. Sci.,* **37,** 2035–2050.

——, and W.-K. Tao, 1980: Response of deep tropical cumulus clouds to mesoscale processes. *J. Atmos. Sci.,* **37,** 2016–2034.

——, and ——, 1984: A numerical study of the vertical transport of momentum in a tropical rainband. *J. Atmos. Sci.,* **41,** 1049–1061.

Steiner, M., R. A. Houze Jr., and S. E. Yuter, 1995: Climatological characterization of three-dimensional storm structure from operational radar and rain gauge data. *J. Appl. Meteor.,* **34,** 1978–2007.

Sui, C. H., K. M. Lau, W. K. Tao, and J. Simpson, 1994: The tropical water and energy cycles in a cumulus ensemble model. Part I: Equilibrium climate. *J. Atmos. Sci.,* **51,** 711–728.

Tao, W.-K., and S.-T. Soong, 1986: A study of the response of deep tropical clouds to mesoscale processes: Three-dimensional numerical experiments. *J. Atmos. Sci.,* **43,** 2653–2676.

——, and J. Simpson, 1989: Modeling study of a tropical squall-type convective line. *J. Atmos. Sci.,* **46,** 177–202.

——, and ——, 1993: The Goddard cumulus ensemble model. Part I: Model description. *Terr. Atmos. Oceanic Sci.,* **4,** 35–72.

——, ——, C. H. Sui, B. Ferrier, S. Lang, J. Scala, M. D. Chou, and K. Pickering, 1993: Heating, moisture, and water budgets of tropical and midlatitude squall lines: Comparisons and sensitivity to longwave radiation. *J. Atmos. Sci.,* **50,** 673–690.

——, S. Lang, J. Simpson, C.-H. Sui, B. Ferrier, and M.-D. Chou, 1996: Mechanisms of cloud–radiation interaction in the Tropics and midlatitudes. *J. Atmos. Sci.,* **53,** 2624–2651.

——, J. Simpson, C.-H. Sui, C.-L. Shie, B. Zhou, K. M. Lau, and M. Moncrieff, 1999: Equilibrium states simulated by cloud-resolving models. *J. Atmos. Sci.,* **56,** 3128–3139.

——, C.-L. Shie, J. Simpson, S. Braun, R. H. Johnson, and P. E. Ciesielski, 2003a: Convective systems over the South China Sea: Cloud-resolving model simulations. *J. Atmos. Sci.,* **60,** 2929–2956.

——, and Coauthors, 2003b: Microphysics, radiation and surface processes in the Goddard Cumulus Ensemble (GCE) model. *Meteor. Atmos. Phys.,* **82,** 97–137.

——, D. Johnson, C.-L. Shie, and J. Simpson, 2004: The atmospheric energy budget and large-scale precipitation efficiency of convective systems during TOGA COARE, GATE, SCSMEX, and ARM: Cloud-resolving model simulations. *J. Atmos. Sci.,* **61,** 2405–2423.

——, and Coauthors, 2008: A multi-scale modeling system: Development, applications, and critical issues. *Bull. Amer. Meteor. Soc.,* in press.

Tripoli, G. J., 1992: A nonhydrostatic mesoscale model designed to simulate scale interaction. *Mon. Wea. Rev.,* **120,** 1342–1359.

Wang, Y., W.-K. Tao, and J. Simpson, 1996: The impact of ocean surface fluxes on a TOGA COARE convective system. *Mon. Wea. Rev.,* **124,** 2753–2763.

Weisman, M. L., and J. B. Klemp, 1982: The dependence of numerically simulated convective storms on vertical wind shear and buoyancy. *Mon. Wea. Rev.,* **110,** 504–520.

Wielicki, B. A., B. R. Barkstrom, E. F. Harrison, R. B. Lee III, G. L. Smith, and J. E. Cooper, 1996: Clouds and the Earth's Radiant Energy System (CERES): An Earth Observing System experiment. *Bull. Amer. Meteor. Soc.,* **77,** 853–868.

Wu, X., W. W. Grabowski, and M. W. Moncrieff, 1998: Long-term behavior of cloud systems in TOGA COARE and their interactions with radiative and surface processes. Part I: Two-dimensional modeling study. *J. Atmos. Sci.,* **55,** 2693–2714.

——, W. D. Hall, W. W. Grabowski, M. W. Moncrieff, W. D. Collins, and J. T. Kiehl, 1999: Long-term behavior of cloud systems in TOGA COARE and their interactions with radiative and surface processes. Part II: Effects of ice microphysics on cloud–radiation interaction. *J. Atmos. Sci.,* **56,** 3177–3195.

Xie, S., and Coauthors, 2005: Simulations of midlatitude frontal clouds by single-column and cloud-resolving models during the Atmospheric Radiation Measurement March 2000 cloud intensive operational period. *J. Geophys. Res.,* **110,** D15S03, doi:10.1029/2004JD005119.

Xu, K.-M., 1995: Partitioning mass, heat, and moisture budgets of explicitly simulated cumulus ensembles into convective and stratiform components. *J. Atmos. Sci.,* **52,** 551–573.

——, and D. A. Randall, 1996: Explicit simulation of cumulus ensembles with the GATE Phase III data: Comparison with observations. *J. Atmos. Sci.,* **53,** 3710–3736.

——, and Coauthors, 2002: An intercomparison of cloud-resolving models with the ARM summer 1997 IOP data. *Quart. J. Roy. Meteor. Soc.,* **128,** 593–624.

——, and Coauthors, 2005: Modeling springtime shallow frontal clouds with cloud-resolving and single-column models. *J. Geophys. Res.,* **110,** D15S04, doi:10.1029/2004JD005153.

Yuter, S. E., and R. A. Houze, 1995: Three-dimensional kinematic and microphysical evolution of Florida cumulonimbus. Part II: Frequency distributions of vertical velocity, reflectivity, and differential reflectivity. *Mon. Wea. Rev.,* **123,** 1941–1963.

Zeng, X., and Coauthors, 2007: Evaluating clouds in long-term cloud-resolving model simulations with observational data. *J. Atmos. Sci.,* **64,** 4153–4177.